

Scale-up fabrication and characteristic study of oligomer-like small-molecule solar cells by ambient halogen-free sheet-to-sheet and roll-to-roll slot-die coating

Yun-Ming Sung^{a,b}, Cheng-Si Tsao^{a,c,*}, Hua-Kai Lin^a, Hou-Chin Cha^a, Yu-Ching Huang^{d,*}

^a Institute of Nuclear Energy Research, Longtan, Taoyuan 32546, Taiwan

^b Institute of Atomic and Molecular Science, Academia Sinica, Taipei 106, Taiwan

^c Department of Material Science and Engineering, National Taiwan University, Taipei 106, Taiwan

^d Department of Materials Engineering, Ming Chi University of Technology, New Taipei City 24301, Taiwan

ARTICLE INFO

Keywords:

Organic solar cells
Small molecule
Slot-die
Large-area
Photo-stability

ABSTRACT

The upscale fabrication of the inverted small-molecule organic solar cell (SMOSC) from spin coating to large-area slot-die coating using halogen-free solvent under the ambient air environment is developed. This work successfully adopts thermal annealing treatment to tune the bulk heterojunction (BHJ) structure for two advantages of compatibility to mass production and good photo-stability. By tuning the respective optimum film structure, the power conversion efficiency (PCE) values under AM 1.5G light and indoor light (T5 lamp with 500 lx) illuminations for the ambient spin-coated device achieve 8.5% and 13.26%, respectively. The photo-bleaching and light-soaking tests under the AM 1.5G illumination show that the photo-stability of the thermally-annealed DRCN5T:PC₇₁BM device is much better than PTB7-Th:PC₇₁BM device. The tunable BHJ film morphologies of large-area ITO/glass-based sheet-to-sheet (S2S) and flexible roll-to-roll (R2R) slot-die coatings of DRCN5T:PC₇₁BM SMOSCs are based on different dry-film formation and crystallization mechanisms. The structural control during the drying-film process for S2S and R2R coatings is a critical key to determine the optimum performance. The PCEs of the ITO/glass-based and flexible ITO/PET-based SMOSCs achieve 7.6% and 7.3%, respectively. The PCE of the ambient flexible R2R slot-die-coated SMOSC using halogen-free solvent is much higher than that of the currently flexible R2R coated SMOSCs. The PCEs of S2S slot-die-coated cell device of 1 × 5 cm² and module achieve 5.1%. We conduct a characteristic, structural and systematic study of how to scale-up SMOSC via slot-die coatings, demonstrating the relationship among processing control, performance and structure for different coatings.

1. Introduction

Solution-processed bulk heterojunction (BHJ) organic solar cells (OSCs) have attracted a large number of interests due to its advantages of low cost, lightweight, flexibility, roll-to-roll (R2R) compatibility and easy production (Krebs et al., 2009; Søndergaard et al., 2012; Gu et al., 2017). Recently, the rapid progress of power conversion efficiency (PCE) for the polymer-based OSC (P-OSCs) achieved 18.4% (Lin et al.). Compared to the widely-investigated P-OSCs (Yuan et al., 2019; Pan et al., 2019; Ma et al., 2020; Liu et al., 2020; Chang et al., 2021; Lee et al., 2020), solution-processed small-molecule organic solar cells (SMOSCs) have made great strides and recently achieved a remarkable PCE of 16.28% for ternary SMOSC (Jiang et al., 2021). OSCs are

considered as a promising solar energy conversion technology. Apart from the improvement of polymer or small-molecule donor materials, the BHJ structure or morphological control of the active layer of OSCs plays an important role in PCE (Huang et al., 2013; Liu et al., 2013; Liao et al., 2014; Li et al., 2020; An et al., 2020; Song et al., 2020; Zhang et al., 2020; Farahat et al., 2016; Love et al., 2013; Kyaw et al., 2014; Min et al., 2016; Collins et al., 2017; Yue et al., 2019). The BHJ structure is a nano-scale interpenetration network of donor and acceptor phases which is closely related the exciton generation, charge separation at interface and charge transportation. The BHJ structure is formed in the complex phase separation during film processing and drying process. To date, several strategies effectively control the BHJ morphology and thus improve PCE are reported in a large number of literatures, including

* Corresponding authors.

E-mail addresses: cstsao@iner.gov.tw (C.-S. Tsao), huangyc@mail.mcut.edu.tw (Y.-C. Huang).

<https://doi.org/10.1016/j.solener.2021.11.080>

Received 30 August 2021; Received in revised form 19 November 2021; Accepted 30 November 2021

Available online 11 December 2021

0038-092X/© 2021 International Solar Energy Society. Published by Elsevier Ltd. All rights reserved.

solvent additives, thermal annealing (TA) and solvent vapor annealing (SVA), etc. Compared to P-OSCs, SMOSCs have several advantages, including high purity, easy purification, no batch-to batch variation, well-defined chemical structure and easy to change its energy level, etc. The solution-processed SMOSC research (Qin et al., 2020; Ge et al., 2021; Guijarro et al., 2020; Xiao et al., 2021) has been substantially focused and developed in parallel to P-OSCs research.

Among the various kinds of small molecules, the acceptor–donor–acceptor (A-D-A) structure is one of the more successful structure due to the feasibility of tuning its energy level and absorption spectrum (Chen et al., 2013; Wessendorf et al., 2014; Feng et al., 2017). The oligothiophenes is a well-studied organic material in A-D-A structure because of its tunable absorption spectrum and energy level, high stability, good charge transport and simple synthesis process (Fitzner et al., 2012; Zhang et al., 2014; Duan et al., 2020; Lee et al., 2020). A series of A-D-A oligothiophenes of DRCN4T-DRCN9T was reported by Kan and co-workers, the PCE of SMOSC using DRCN5T as donor can achieve 10.08% by finely tuning the BHJ structure via TA or SVA treatment (Kan et al., 2015). The industrial figure of merit (Min et al., 2017) pointed out that the performance, photo-stability and synthetic complexity of DRCN5T is one of the most desirable SMOSC materials for realizing commercialization. Although these SMOSCs with high PCE were developed, they were laboratory-scale and prepared with halogen-containing solvent under nitrogen environment. There is a large gap in the development of fabrication processing between laboratory-scale spin coating and large-area slot-die coating toward commercialization of SMOSC. For the formation of BHJ structure, the previous study (Huang et al., 2015) using small-angle and wide-angle X-ray scattering on SMOSCs pointed out that the crystallinity and crystallization kinetics of small-molecule donor are largely different to those of polymer donor. The formation mechanism of BHJ structure and crystallization kinetics is also different for different coating process, hence, the upscaling study of SMOSC using the halogen-free solvent under the ambient air environment is necessary but still limited to date.

The ambient R2R slot-die coating for flexible SMOSC using halogen-containing solvent was reported firstly by Lin et al. (2013). Heo et al. adopted the halogen-free solvent and ambient S2S slot-die coating for fabricating BTR:PC₇₁BM-based SMOSC and the PCE of SMOSC device achieved 7.46% by using SVA treatment for tuning BHJ structure (Heo et al., 2017). The studies on R2R slot-die-coated SMOSC are very few. According to the previous study on flexible large-area R2R slot-die coating of P-OSCs (Huang et al., 2016), the BHJ morphology initial formed during the film drying process is closely related to the drying temperature of R2R oven. The control of the initial BHJ morphology plays the same important role in performance to that of final BHJ structure controlled by the subsequent TA or SVA treatment. The relatively limited research of upscaling SMOSC compared to P-OSCs motivated us systematically investigate how to optimally upscale the spin-coating to ambient large-area glass-based S2S and flexible R2R slot-die coatings by morphological control and halogen-free solvent. The characteristic study for the variation in PCE under indoor lighting and light-induced degradation is also included here.

In the present study, we focus on the upscale fabrication of DRCN5T:PC₇₁BM SMOSC from spin coating to large-area slot-die coating using oxygen solvent under the ambient air environment. The only TA treatment is adopted here based on two reasons: (1) TA is simpler and more compatible to mass production than SVA. (2) The photo-stability of DRCN5T-based SMOSC treated with TA is much higher than that treated SVA (Min et al., 2016; Min et al., 2017). In the spin coating process, the devices exhibit the PCE of 8.5% and 13.26% under AM1.5G and indoor light (T5 lamp with 500 lx) illumination, respectively. The photo-induced device degradation under AM-1.5G illumination is also investigated. For the ITO/glass-based S2S and flexible ITO/PET-based R2R slot-die coating, we tune the morphology and crystallization of DRCN5T:PC₇₁BM active layer by film drying process and TA treatment finally to achieve an optimum structure and performance. PCEs of the SMOSC

devices prepared with ITO/glass-based S2S and flexible ITO/PET-based R2R slot-die coatings achieve 7.6% and 7.3%, respectively. They are comparable to the PCE (7.46%) of ITO/glass-based S2S slot-die-coated and SVA-treated BTR:PC₇₁BM SMOSC previously reported. The slot-die-coated SMOSC treated by TA demonstrates much better photostability than the PTB7:PC₇₁BM P-OSC at the same light soaking (AM1.5G) experiment. The PCEs of S2S slot-die-coated cell (active area: 1 × 5 cm²) and module are 5.1% and 5.1%, respectively. To our knowledge, the PCE of ambient flexible R2R slot-die coating of SMOSC using halogen-free solvent reported in this work is the highest among all flexible R2R coated SMOSCs. Each coating process has different film formation mechanism. We conduct a characteristic, structural and systematic study of how to scale-up SMOSC via glass-based S2S slot-die coating and flexible R2R slot-die coating, demonstrating the relationship between processing control, performance and structure for different coatings. The results provide the useful information for realizing the SMOSC low-cost mass production and commercialization.

2. Experiment

2.1. Materials

The ITO-coated glass with sheet resistance of 5 Ω/□ was purchased from Luminescence Technology Corporation. The flexible ITO/PET with a sheet resistance of 15 Ω/□ was purchased from Vestech Taiwan Corporation. All solvents used in this research were purchased from Sigma-Aldrich. DRCN5T and PC₇₁BM were purchased from 1-materials and Nano-C, respectively. The synthesis of ZnO nanoparticles was followed the literature reported by Wang et al. (2007). MoO₃ and silver were purchased from Gredmann corporation. The DRCN5T:PC₇₁BM solution with the ratio of 1:0.8 was stirred at 70 °C for 1 day in glove box.

2.2. Spin-coated device fabrication

The ITO glasses were wiped by acetone and isopropanol and then dried by flowing nitrogen gas. After previous cleaning process, the ITO glasses were also cleaned by O₂ plasma for 10 min. The 10 mg/mL ZnO nanoparticles solution was spin-coated on ITO glasses at 5000 rpm for 30 s. The DRCN5T:PC₇₁BM solution with the blending ratio of 1:0.8 and total concentration of 36 mg/mL was spin-coated on previous substrates at 1000 rpm for 40 s in ambient air and then followed by annealing at 120 °C for 10 min. The resulted thickness of DRCN5T:PC₇₁BM layer was 100 nm. After that, the devices were completed by thermally evaporated 8 nm MoO₃ and 100 nm silver on active layer with the rate of 0.3 Å/s and 1 Å/s under 5 × 10⁻⁶ torr. The resulted device area was 0.3 cm².

2.3. Sheet to sheet (S2S) coated device fabrication

The ITO glass was cut to 7 × 10 cm² and then followed by the same cleaning process as spin-coated devices. Then, 30 nm ZnO nanoparticles layer was deposited on ITO glass by slot-die coater with the coating speed and flow rate of 0.5 m/min and 0.45 ml/min. For active layer coating process, the DRCN5T:PC₇₁BM solution with the total concentration of 36 mg/mL was coated on the ZnO-coated substrate under different temperatures and then annealed at 120 °C for 10 min in oven. The resulted thickness of DRCN5T:PC₇₁BM layer was 100 nm. All the S2S coating processes and thermal annealing were conducted in air. After the solution coating processes, the devices were completed by the same top electrode deposition.

2.4. Roll to roll (R2R) coated device fabrication

The 15 Ω/□ flexible ITO/PET was wiped by acetone and then mounted on the roller in R2R coating equipment. Then, the substrates were cleaned by plasma cleaner at the speed of 0.5 m/min. ZnO nanoparticles layer was deposited on cleaned ITO/PET with the coating speed

and flow rate of 0.5 m/min and 0.45 ml/min by slot-die coater and then dried by an oven in R2R coating equipment with the temperature and length of 130 °C and 0.5 m. Then, DRCN5T:PC₇₁BM solution with the total concentration of 18 mg/mL was coated on ZnO-coated substrate and then dried by the same oven. The resulted thickness of DRCN5T:PC₇₁BM layer was 100 nm. After the coating process, the coated ITO/PET was unloaded from the R2R coating equipment and then annealed at 120 °C in oven. All the R2R coating processes and thermal annealing were conducted in air. The devices were completed by the same top electrode deposition.

2.5. Characteristic

The current-voltage measurement of the un-encapsulated devices was conducted in air under AM1.5G light illumination from a solar simulator (Abet Technologies). The AFM images were measured by a desktop AFM instrument (Innova, Bruker). The UV-visible absorption spectrum was measured by an UV-visible spectrophotometer (V-770, JASCO). The impedance measurements were conducted under air and dark condition by using impedance spectrum analyzer (Zahner IM6). The measurements were recorded in the frequency range from 1 Hz to 3 MHz with applied DC voltage of 0 V and AC voltage of 20 mV.

3. Results and discussion

The previous studies of DRCN5T:PC₇₁BM SMOSCs were focused on the conventional structure. For improving the stability (Doumon et al., 2019; Hau et al., 2008), we adopt the inverted structure with the architecture of glass- or PET-ITO/ZnO/DRCN5T:PC₇₁BM/MoO₃/Ag (top electrode), as shown in Fig. 1a. In this study, we use ZnO nanoparticles (Krebs et al., 2009; Zhang et al., 2017) as electron transport layer (ETL), having good flexibility and resistance to overcome the shearing force during the roll-to-roll coating process. The energy level alignment of inverted device is also shown in Fig. 1b, exhibiting a cascade energy

level alignment for both electron and hole transportation. The best performance of DRCN5T:PC₇₁BM SMOSCs reported in the literature (Kan et al., 2015) are the spin-coated chloroform-processed devices with the efficiency of 8.19% and 10.08% by TA and TA + SVA treatment for tuning film morphology, respectively. For the target of commercialization, all spin-coating, glass-based S2S slot-die-coating and flexible R2R coating processes are developed based on the green solvent, o-xylene, as the host solvent under the ambient-air condition in this work. Because of o-xylene with relatively low solubility than chloroform, the formation of spin-coated dry film easily suffers the local segregations causing the crack-like topography, as shown in Fig. S1. Crystallization, BHJ morphology and film quality control by the solution viscosity or concentration during fast spin coating plays the important role in PCE in additional to control of film thickness. With the optimum DRCN5T:PC₇₁BM thickness of 100 nm, the variation in photovoltaic performance of spin-coated devices with the used concentration of active-layer solution is shown in Table 1. The corresponding current density–voltage curves and the tendency of the performance with the used concentration are shown in Fig. 1c and d, respectively. The optimum concentration for achieving the best PCE among the devices is 36 mg/ml, showing the best

Table 1

Photovoltaic characteristic of the spin-coated DRCN5T:PC₇₁BM SMOSCs prepared with different concentration of active-layer solution. The data in the bracket are averaged over at least 5 devices per concentration condition.

Concentration (mg/mL)	J _{sc} (mA/cm ²)	V _{oc} (V)	FF (%)	PCE (%)
18	12.64	0.95	53.70	6.50
36	12.13 ± 0.60	0.94 ± 0.01	51.20 ± 2.82	5.83 ± 0.42
45	15.48	0.92	59.30	8.50
	14.98 ± 0.27	0.92 ± 0.01	55.75 ± 1.94	7.74 ± 0.43
	12.36	0.94	44.00	5.10
	11.61 ± 0.82	0.94 ± 0.00	41.99 ± 1.67	4.58 ± 0.46

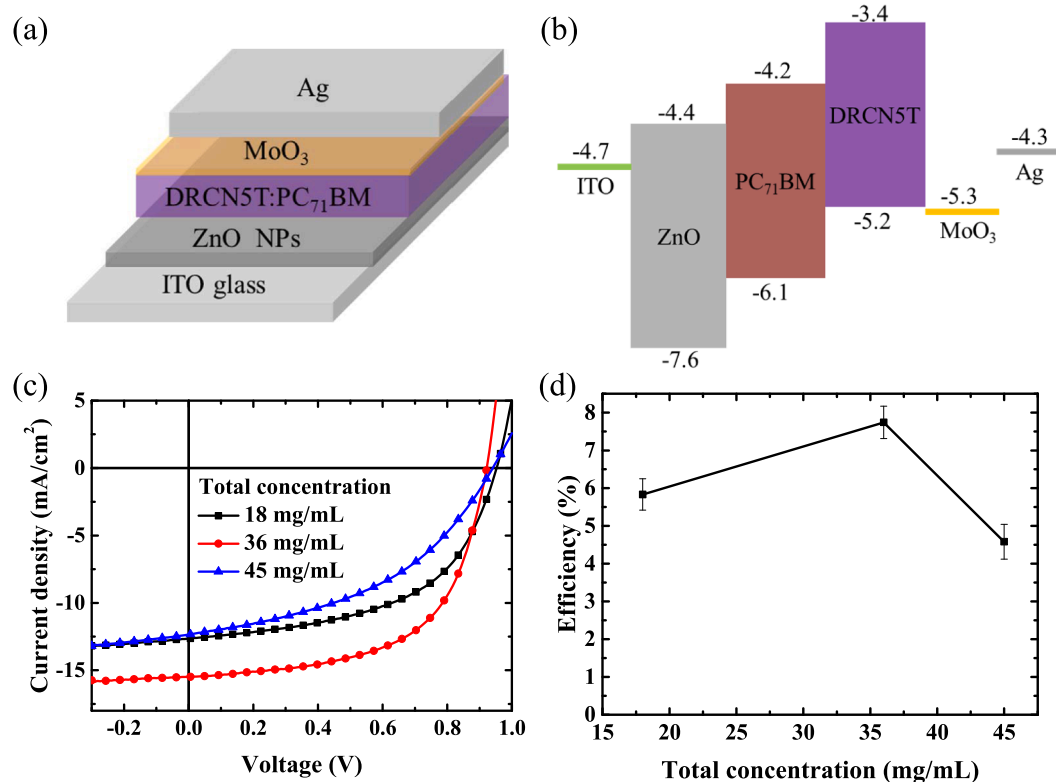


Fig. 1. (a) Inverted SMOSC structure, (b) energy level alignment, (c) current density–voltage curves of the spin-coated devices with the used total concentrations and (d) the corresponding PCE. The devices are prepared with the DRCN5T:PC₇₁BM film thickness of 100 nm.

PCE of 8.5% for the spin-coated device with TA treatment which is higher than the reported PCE (8.19%) of the spin-coated chloroform-processed device with TA treatment. The relatively low performance based on 18 mg/mL and 45 mg/mL of solutions can be attributed to the low J_{sc} and FF which are caused by the poor carrier transport path and recombination. In order to correlate the DRCN5T:PC₇₁BM morphology change with performance, a series of atomic force microscopy (AFM) measurements are carried out for different concentration with and without TA treatment. The results are shown in Fig. 2. The topographies of the un-annealed and annealed films based on 18 mg/ml are shown in Fig. 2a and d, showing many pinholes on their surfaces. The surface roughness slightly increases from 1.12 nm to 1.38 nm after thermal annealing and the spindle-like topography is formed which signifies the slightly improved phase separation. The formation of pin hole may be closely related to the low concentration of the solution and high boiling point of the solvent which cause serious segregation and discontinuous film. After top MoO₃/Ag electrode deposition, MoO₃ and silver would diffuse into the pinhole and then lead to serious recombination. In contrast, the topographies of the un-annealed and annealed films based on 36 mg/ml are shown in Fig. 2b and e, showing no pinholes in both films. The topography of the un-annealed film shows a relative smooth surface with roughness of 0.89 nm and no distinct phase separation. Remarkably, after thermal annealing at 120 °C for 10 min, distinct spindle-like topography and phase separation (a nanoscale bi-continuous network) is observed in topography which is also indicated by the increase of surface roughness to 1.02 nm. The well-separated and fine BHJ structure compared to the films based on the other concentrations indicates that the crystallinity, the interface between two phases and charge transport paths to the respective electrodes are significantly improved. These improvements of BHJ morphology and the smooth film surface (good contact with top electrode) lead to the highest current, FF and PCE of 8.5%. The topographies of the un-annealed and annealed films based on 45 mg/ml are shown in Fig. 2c and f. The surfaces of both films show the existence of many particles and high roughness of 1.06 nm and 1.67 nm for un-annealed and annealed films, respectively. It is speculated that these particles come from the un-dissolved materials which are over the limit of solubility of o-xylene. These particles could lead to poor contact between the active layer and electrode and thus the poor performance compared to other films. The optimum ambient spin-coated device performance and film topography is very similar to the result reported for the chloroform-processed nitrogen-environment spin-coated DRCN5T:PC₇₁BM SMOSC with TA treatment (Kan et al., 2015), showing the feasibility of using o-xylene as host solvent.

Impedance spectroscopy (IS) is used to analyze the information of interfacial interaction and internal electrical properties of the BHJ OSC. Fig. S2(a) shows the Cole-Cole plots of the BHJ devices based on above concentrations of 18, 36 and 45 mg/ml. Fig. S2(b) shows the corresponding imaginary component of impedance–frequency plots. According to the IS study of Tobin et al for BHJ OSC [S1], an equivalent circuit model is used to fit the measured IS data. This circuit model can fit well the IS data in Fig. S2(a) and the fitted results are summarized in Table S1. The fitted parameters are series resistance (R_s), bulk resistance (R_b), geometric capacitor (C_g), chemical capacitor (C_μ), recombination resistance (R_{rec}) and average charge carrier lifetime (τ_{avg}). In Tobin's study, the key parameter is average charge carrier lifetime ($\tau_{avg} = C_\mu \times R_{rec}$) determined by the recombination resistance R_{rec} and chemical capacitor C_μ . The large τ_{avg} value can lead to the high PCE which is closely related to the reduction in recombination in the charge transfer path or interface. The diameter of semicircle in Cole-Cole plot represents the recombination resistance which associates with the charge transfer event at the interface. The increase in τ_{avg} or R_{rec} value could lead to the decrease of the peak frequency in Fig. S2(b) which is also described in the literature [S1]. The device based on the 36 mg/ml has the good morphology and favorable charge transport compared to the other devices, leading to the highest τ_{avg} value of 76.73 μ s and thus the highest PCE of 8.5%. The devices based on 18 and 45 the mg/ml have the poor charge transport and thus the serious recombination due to the existence of local segregation and undissolved particles, respectively. These devices have the reduced τ_{avg} values of 29.88 and 13.95 μ s, leading to the PCE of 6.5% and 5.1%, respectively. The measured τ_{avg} values by IS consistently agree with variation of PCEs.

Generally, SMOSC have excellent PCE under indoor light condition, which is increasingly important for the development of indoor applications (Yin et al., 2018; Lee et al., 2018; Ramirez-Como et al., 2021). It is noteworthy that the thicker DRCN5T:PC₇₁BM layer with the film thickness of 150 nm is required to obtain the optimum PCE under indoor light, which is different from the thickness for the optimum PCE under AM 1.5G light. According to this recipe, the resulted current density–voltage curves of this device and its corresponding characteristics measured under the indoor light and AM1.5G light illuminations are shown in Fig. 3a and Table 2. The prepared DRCN5T:PC₇₁BM SMOSC shows the optimum PCE of 13.26% under the indoor light (T5 lamp with 500 lx) illumination, the PCE of this device measured under the AM1.5G light illumination is 5.1%. The excellent performance under indoor light condition can be attributed to the large shunt resistance and high crystallinity which can reduce carrier recombination (Steim et al., 2011;

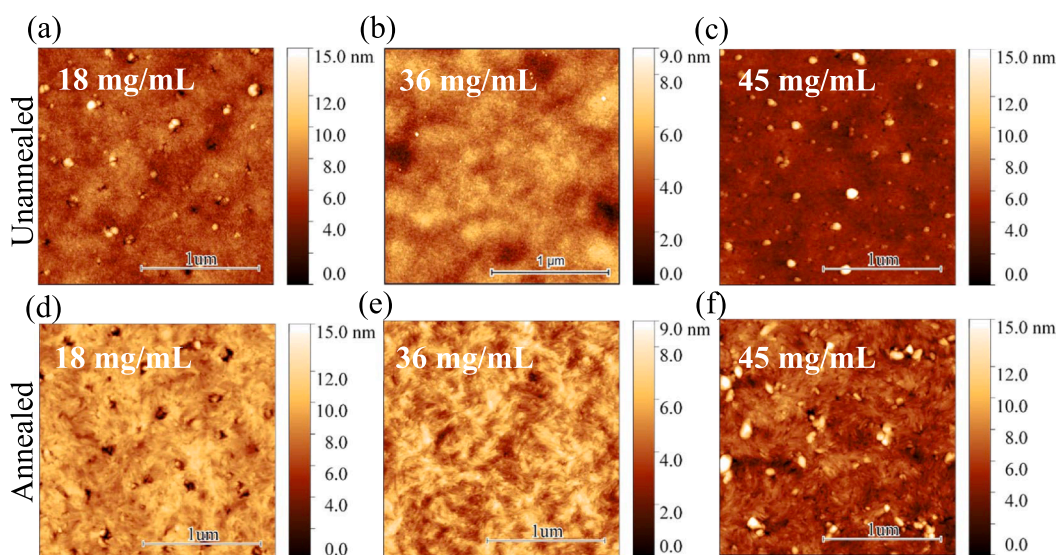


Fig. 2. The topography of spin-coated DRCN5T:PC₇₁BM film of the unannealed and annealed for 10 mins samples with the used total concentration.

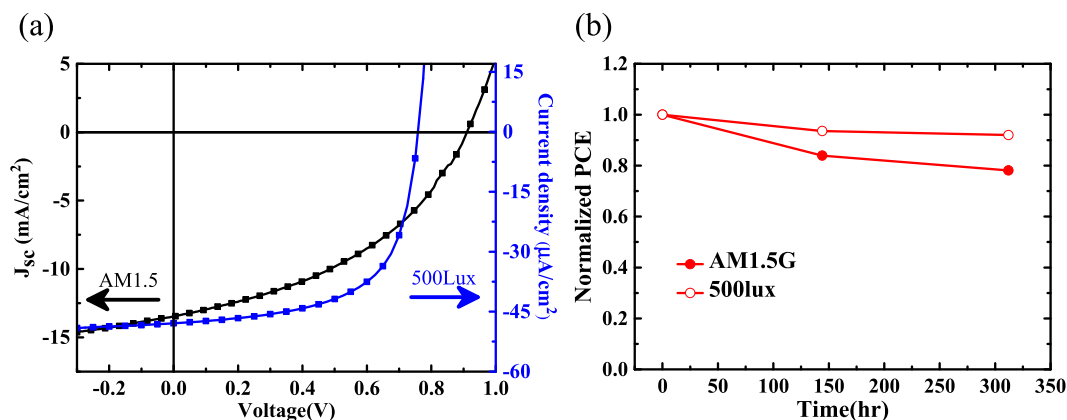


Fig. 3. (a) The current density–voltage curves and (b) the PCE changed with dark storage time of the devices under AM1.5G and 500 lx T5 indoor light illumination. The device is prepared with the DRCN5T:PC₇₁BM thickness of 150 nm for optimum indoor performance.

Table 2

Photovoltaic characteristics of the spin-coated device with the DRCN5T:PC₇₁BM film thickness of 150 nm under AM1.5G and indoor light illumination.

	J_{sc} (mA/cm ²)	V_{oc} (V)	FF (%)	PCE (%)
AM1.5G	13.49	0.91	41.7	5.1
	J_{sc} (μ A/cm ²)	V_{oc} (V)	FF (%)	PCE (%)
Indoor light (T5, 500 lx)	47.93	0.76	62.01	13.26

Proctor and Nguyen, 2015; Park et al., 2018). According to the literature (Lechêne et al., 2016; Miranda et al., 2021), the important parameter to control is the shunt resistance. The shunt resistance could be tuned by the thickness of charge transport layer and active layer. This device without encapsulation also shows good shelf-stability under the dark storage and ambient-air environment, as shown in Fig. 3b. The PCE measured under AM1.5G illumination remains 80% of its initial value after 300 h of ambient dark storage. At the same dark-storage time (300 h), the PCE measured under the indoor light illuminations remains 94% of its initial value.

Photo-bleaching test under the AM1.5G illumination (100 mW/cm²) and ambient air with UV filter is conducted for the unencapsulated (1) PTB7-Th:PC₇₁BM blend film, (2) the un-annealed DRCN5T:PC₇₁BM blend film and (3) the annealed DRCN5T:PC₇₁BM blend film. The absorption spectra of three blend films under 0, 3 and 18 h of continuous illumination are shown in Fig. S3. In Fig. S3a, the absorption intensity of PTB7-Th:PC₇₁BM film rapidly decreases with the continuous light illumination. The absorption peak at 700 nm of PTB7-Th vanishes after 3 h of illumination under ambient air. Both absorption peaks at 600 and 700 nm vanish after 18 h of illumination. The rapidly decreasing absorption intensity and absorption-peak elimination indicate the reduced polymer π - π conjugation which can be attributed to photo-oxidation (Perthué et al., 2018; Löhrer et al., 2020). In Fig. S3b, the DRCN5T:PC₇₁BM film without thermal annealing exhibits absorption peaks at 400 nm and 550 nm, whose peaks can be related to absorption of PC₇₁BM acceptor and DRCN5T donor, respectively. The absorption peak of DRCN5T vanishes after 3 h of continuous illumination under ambient air, suggesting the significant effect of photo-oxidation on the un-annealed DRCN5T:PC₇₁BM blend film. In contrast, the annealed DRCN5T:PC₇₁BM film demonstrates a quite different absorption spectrum with three absorption peaks at 400 nm, 550 nm and 700 nm, as shown in Fig. S3c. The additional absorption peak at 700 nm indicates the increase of crystallinity of DRCN5T after thermal annealing. Furthermore, the photo-bleaching test demonstrates that the annealed DRCN5T:PC₇₁BM film has the more stable absorption spectra which do not change even after 18 h of continuous AM 1.5G light illumination under ambient air. The excellent resistance to photo-oxidation effect can

be attributed to the improved crystallinity which increases π - π conjugation and decreases oxidation of chemical bond. The photo-bleaching test shows that the photo-stability of the annealed DRCN5T:PC₇₁BM film is much better than PTB7-Th:PC₇₁BM film under ambient air. The literatures (Mateker et al., 2015; Yi et al., 2020) pointed out that the increase of crystallinity of P-OSC and SMOSC could effectively improve the resistance to photo-induced degradation. It is interesting to further examine the photo-induced degradation behaviors of both the PTB7-Th:PC₇₁BM P-OSC and the annealed DRCN5T:PC₇₁BM SMOSC prepared in this work. The variation in PCE of both the un-encapsulated P-OSC and SMOSC with the continuous AM 1.5G light (100 mW/cm²) illumination in air is shown in Fig. S1d. The PCEs of the un-encapsulated PTB7-Th:PC₇₁BM P-OSC and the annealed DRCN5T:PC₇₁BM SMOSC drop to 80% of their initial values after 4 h and 75 h (corresponding to T_{80} lifetime), respectively. Remarkably, the photo-induced degradation curve of annealed DRCN5T:PC₇₁BM SMOSC after 75 h shows a stable behavior, suggesting the much better long-term stability than PTB7-Th:PC₇₁BM P-OSC. The light-soaking result of OSC devices is consistent with the result of photo-bleaching test of active layer films.

For upscaling, we develop the S2S large-area slot-die coating of glass-substrate DRCN5T:PC₇₁BM SMOSC by tuning BHJ film morphology based on a different dry film formation and crystallization mechanism. The ambient slot-die coating with the respective optimum film thickness (80–100 nm) are optimized by the different coating parameters (flow rate of unit: ml/min, coating speed of unit: m/min) for the substrate temperatures at 50 °C (0.6 ml/min, 0.5 m/min), 60 °C (1.5 ml/min, 0.5 m/min), 70 °C (0.6 ml/min, 0.5 m/min) and 80 °C (0.9 ml/min, 0.5 m/min). The photovoltaic parameters for each substrate temperature are listed in Table 3. Their current density–voltage curves are shown in Fig. 4. The device coated at the optimum substrate temperature of 60 °C shows the best PCE of 7.6% and the highest J_{sc} of 14.79 mA/cm² compared to the devices coated at the other different

Table 3

Photovoltaic characteristics of the annealed S2S slot-die coated devices with different substrate temperature. The data in the bracket are averaged over at least 5 devices per temperature.

Substrate temperature (°C)	J_{sc} (mA/cm ²)	V_{oc} (V)	FF (%)	PCE (%)
50	13.54	0.94	52.00	6.60
	13.34 ± 0.33	0.93 ± 0.01	49.68 ± 2.49	6.18 ± 0.33
60	14.79	0.93	55.70	7.60
	14.68 ± 0.09	0.93 ± 0.00	53.87 ± 1.13	7.32 ± 0.20
70	12.33	0.93	51.50	5.90
	11.78 ± 0.51	0.92 ± 0.01	51.70 ± 0.82	5.63 ± 0.31
80	4.38	0.51	48.00	1.10
	4.79 ± 0.58	0.39 ± 0.16	37.30 ± 15.13	0.75 ± 0.49

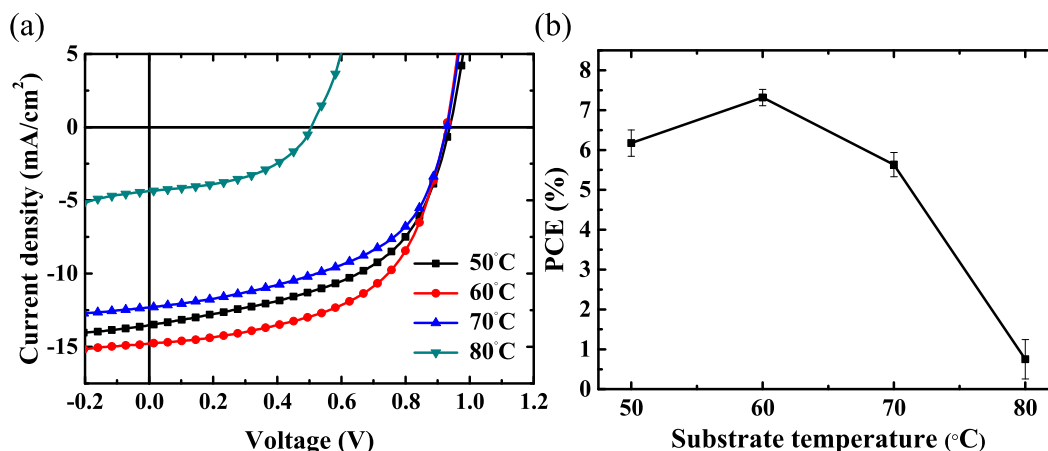


Fig. 4. (a) The current density–voltage curves with different substrate temperatures and (b) corresponding PCE of the S2S slot-die coated devices.

substrate temperatures. This PCE value is comparable to the PCE (7.46%) of S2S slot-die-coated and SVA-treated BTR:PC₇₁BM SMOSC previously reported (Heo et al., 2017). The performance drops rapidly for the substrate temperatures over 60 °C. The efficiency drop can be attributed to difference of the active layer morphology. The substrate temperature controlled by metal heating plate (i.e., a drying temperature) during dry film formation from the wet state to dry state involves interaction including the slow solvent evaporation, DRCN5T crystallization and PC₇₁BM aggregation. The nucleation and initial growth kinetics of the drying process govern the final BHJ structure. The substrate temperature affects the drying time (or solvent evaporation) and thus film crystallinity in addition to thermal annealing in oven, increasing the complexity of morphology control. The previous study indicates the initial drying process of slot-die-coated film could play an important role in control of the BHJ film morphology of the R2R-coated polymer solar cells (Huang et al., 2016). A similar phenomenon is found here to the

S2S slot-die-coated SMOSCs. This effect is also reflected by the absorption spectrum in Fig. S4 which has been normalized by the value of the peak around 500–600 nm. The absorption spectrum for the substrate temperature of 60 °C shows a significant red shift of absorption peak from 560 nm to 532 nm compared to that for the other substrate temperatures. The peak shift suggests the crystallinity due to the substrate temperature of 60 °C is better than that due to the other substrate temperatures; leading to the highest current. The annealed DRCN5T:PC₇₁BM film topographies measured by AFM for different substrate temperatures consistently support this result, as shown in Fig. 5. The film topography based on the substrate temperature of 50 °C shows well-phase-separated and distinct spindle-like topography with the roughness of 1.08 nm, suggesting the substantial crystallization of DRCN5T and PC₇₁BM aggregation. For the substrate temperature of 60 °C, the topography shows the fine phase-separated and spindle-like topography with uniform surface of the roughness of 1.05 nm. The substrate

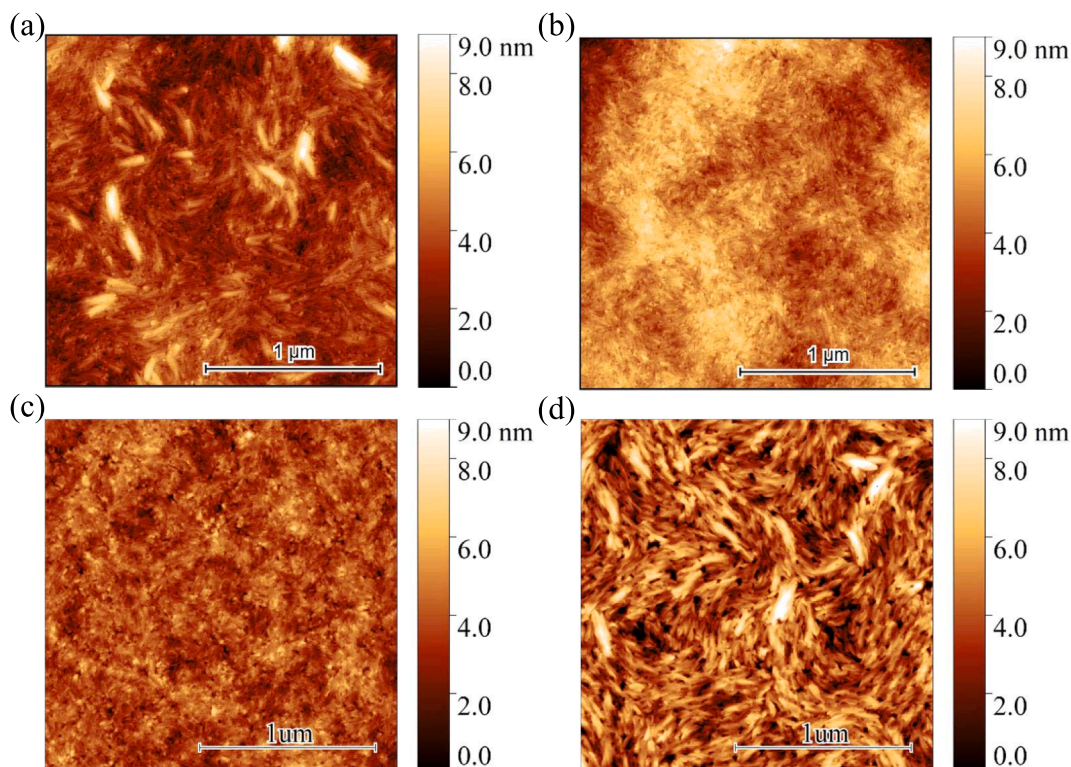


Fig. 5. The annealed film topography of S2S slot-die coated DRCN5T:PC₇₁BM film with the substrate temperatures of (a) 50 °C (b) 60 °C, (c) 70 °C and (d) 80 °C.

temperature of 60 °C enables not only forming highest SM crystallinity and favorable BHJ network with large interface between acceptor and donor phases comparing to the results under other substrate temperatures, but also good contact with top electrode due to its uniform surface, exhibiting the highest PCE. The topography based on the substrate temperature of 70 °C shows a fine phase-separated structure with the roughness of 0.89 nm but some pinholes on its surface which leads to the large decrease in PCE. The topography based on the substrate temperature of 80 °C shows the coarsened BHJ structure with roughness of 1.59 nm and more pinholes, leading to serious carrier recombination and thus dramatic drop of PCE. Based on these results, the control of substrate temperature during the drying process is a critical key to determine the phase-separated BHJ morphology, SM crystallinity, film thickness and photovoltaic performance. For assessing the uniformity of the coated film, the cell device with the active area of $1 \times 5 \text{ cm}^2$ and the 8-cell module with active area of 3.2 cm^2 (each cell area: $1 \times 0.4 \text{ cm}^2$) are fabricated according to this ambient S2S slot-die-coated process with o-xylene as host solvent. The corresponding current density–voltage curves and performance are shown in Fig. S5 and Table S2. The cell device of $1 \times 5 \text{ cm}^2$ exhibits the J_{sc} of 12.56 mA/cm^2 , V_{oc} of 0.95 V, FF of 42.74% and PCE of 5.1 %. The drop in PCE due to the area upscaling can be mainly attributed to (1) the ohmic loss caused by the high resistance of ITO, and (2) the non-uniform thickness and local heterogeneity of the DRCN5T:PC₇₁BM layer. The module demonstrates the J_{sc} of 1.71 mA/cm^2 , V_{oc} of 6.61 V, FF of 45.30% and PCE of 5.1 %. The PCE loss of module may be due to the defect factors of series connection between cells, such as P1 laser ablation and P2 ablation. Hence, the better PCE of the large-area cell and module can be achieved by using (1) low resistance of ITO, (2) correction of P1 and P2 ablation and (3) finely-tuned BHJ structure in the future.

Furthermore, the flexible ambient R2R slot-die coated process of DRCN5T:PC₇₁BM SMOSC based ITO/PET substrate is developed. It is noteworthy that the suitable film-formation mechanism of R2R slot-die coating is largely different from that of glass-substrate S2S slot-die coating because of (1) drying process by hot air within the on-line oven with a length: 0.5 m and (2) consideration of stress and strain of moving flexible layers. The low DRCN5T:PC₇₁BM concentration of 18 mg/ml is more favorable than other concentrations because the thin film could be rapidly dried and avoid the large roughness. The optimum drying temperature of the hot air (130 °C) with combination of coating speed (0.5 m/min) can provide the main influence in the initial crystallization which is similar to the R2R polymer-based OSCs and S2S slot-die coated SMOSC (Huang et al., 2016). The flexible R2R slot-die-coated DRCN5T:PC₇₁BM film thickness is 100 nm. The corresponding J-V curves for the devices with and without additional 15 mins thermal annealing are shown in Fig. 6a. The results of PCE changed with additional annealing time are shown in Fig. 6b. As shown in Table 4, the device without additional thermal annealing shows PCE of 5.40%. The additional thermal annealing at 120 °C in a static off-line oven for 15 mins can greatly improve PCE up to 7.3%. The additional thermal annealing plays an important role in tuning PCE, final SM crystallization and BHJ morphology. The topography of the optimized R2R-coated DRCN5T:PC₇₁BM film annealed for 15 min, as shown in Fig. 6c, exhibits the different topography to the optimum S2S-coated film and has the much smaller roughness of 0.45 nm. The small spindle- and particle-like topography indicate a quite different morphology formation. The reason may be attributed to the thin, homogeneous and uniform film deposited using the low concentration of DRCN5T:PC₇₁BM solution, different drying process and the shearing force of the flexible substrate. These results again emphasize the effects of the different coating process

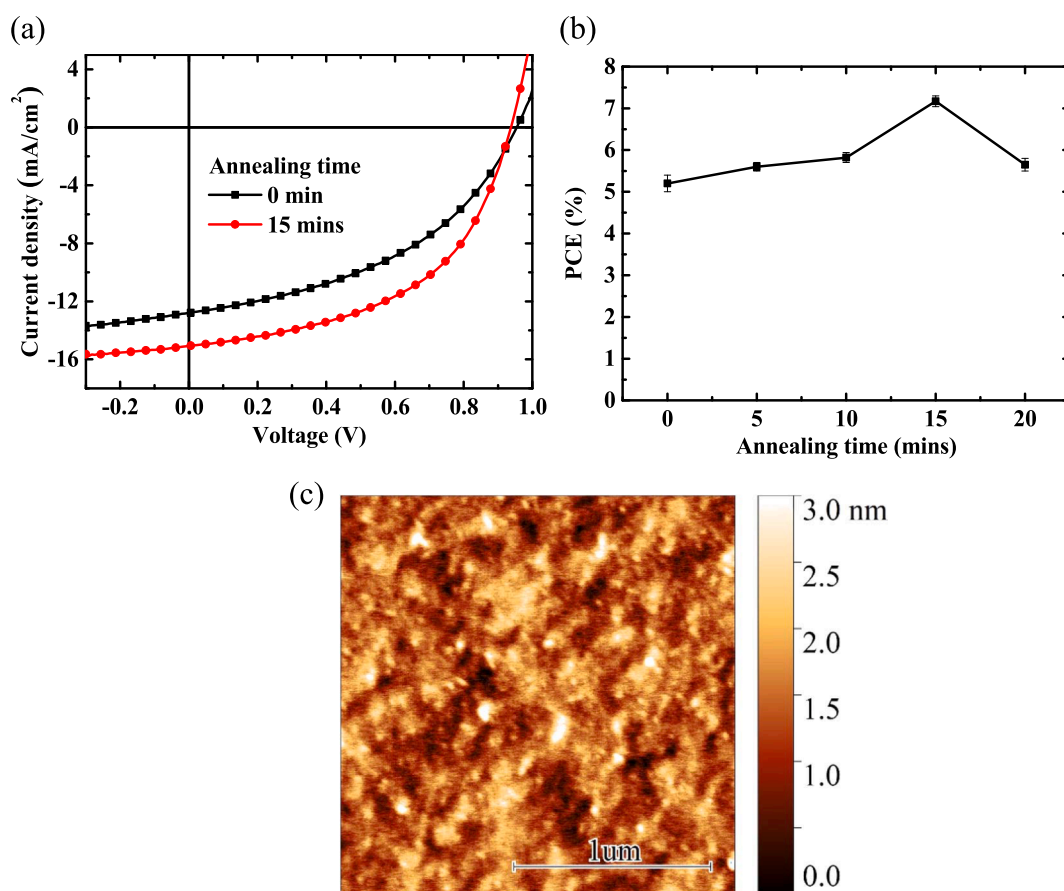


Fig. 6. The R2R slot-die coated devices' (a) the current density–voltage curves of the devices without and with annealing for 15 mins, (b) PCE changed with various devices annealing time and (c) topography of the optimized DRCN5T:PC₇₁BM film.

Table 4

The characteristics of the R2R slot-die coated devices with different annealing time. The data in the bracket are averaged over at least 5 devices per annealing time.

Annealing time (mins)	J_{sc} (mA/cm ²)	V_{oc} (V)	FF (%)	PCE (%)
0	12.80	0.95	43.90	5.40
5	11.56 ± 1.24	0.95 ± 0.00	41.50 ± 2.40	4.60 ± 0.80
	12.28	0.94	50.50	5.80
10	12.19 ± 0.06	0.93 ± 0.01	50.28 ± 0.46	5.73 ± 0.04
	12.43	0.94	51.80	6.00
15	12.95 ± 0.78	0.93 ± 0.00	48.50 ± 3.61	5.82 ± 0.11
	15.04	0.94	51.40	7.30
20	14.91 ± 0.21	0.94 ± 0.00	51.07 ± 0.25	7.17 ± 0.13
	13.31	0.92	47.80	5.80
	13.79 ± 0.48	0.92 ± 0.00	44.60 ± 3.2	5.65 ± 0.15

and dry process for the film morphology formation.

4. Conclusion

The upscale fabrication of the inverted DRCN5T:PC₇₁BM SMOSC from spin coating to large-area slot-die coating using o-xylene solvent under the ambient air environment is developed. This work successfully adopts TA treatment instead of the well-used SVA treatment to tune the BHJ structure due to two advantages of compatibility to mass production and good photo-stability. By tuning BHJ structure, the PCE of 8.5% for the ambient spin-coated device with TA treatment is comparable to the reported PCE (8.19%) of the spin-coated N₂-environment chloroform-processed device with TA treatment. The PCE of the DRCN5T:PC₇₁BM SMOSC with the respective optimum film structure can achieve the 13.26% under the indoor light (T5 lamp with 500 lx) illumination. The excellent resistance to photo-oxidation effect can be attributed to the improved crystallinity. The photo-bleaching and light-soaking tests under the AM 1.5G light illumination show that the photo-stability of the thermally-annealed DRCN5T:PC₇₁BM device is much better than PTB7-Th:PC₇₁BM device under ambient air. The tunable BHJ film morphology of large-area S2S slot-die coating of ITO/glass-based DRCN5T:PC₇₁BM SMOSC is based on a different dry film formation and crystallization mechanism. The control of substrate temperature during the drying-film process is a critical key to determine the phase-separated BHJ morphology, SM crystallinity, film thickness and photovoltaic performance. The device coated at the substrate temperature of 60 °C shows the best PCE of 7.6% which is comparable to the PCE (7.46%) of S2S slot-die-coated and SVA-treated BTR:PC₇₁BM SMOSC previously reported. The S2S coated cell device of 1 × 5 cm² exhibits the PCE of 5.1 %. The 8-cell module exhibits the PCE of 5.1 %. The film-formation mechanism of flexible R2R slot-die-coated ITO/PET-based DRCN5T:PC₇₁BM SMOSCs is largely different from that of S2S slot-die coating because drying process is controlled by hot air within the on-line oven. The optimum drying temperature of the hot air (130 °C) with combination of coating speed (0.5 m/min) and solution concentration can provide the main influence in the initial crystallization. The additional thermal annealing at 120 °C for 15 mins could greatly improve PCE up to 7.3%. This work provides the meaningful information of upscaling fabrication and performance control of SMOSC toward mass production.

Declaration of Competing Interest

The authors declare that they have no known competing financial interests or personal relationships that could have appeared to influence the work reported in this paper.

Acknowledgements

We would like to thank Dr. Juen-Kai Wang for valuable discussion.

This work was supported by Ministry of Science and Technology of Taiwan (MOST 107-2218-E-131-007-MY3, MOST 110-2221-E-131-010, MOST 110-2622-E-131-011), and Academia Sinica (AS-SS-109-05).

Appendix A. Supplementary material

Supplementary data to this article can be found online at <https://doi.org/10.1016/j.solener.2021.11.080>.

References

- An, K., Zhong, W., Ying, L., 2020. Enhanced performance of P3HT-based non-fullerene polymer solar cells by optimizing film morphology using non-halogenated solvent. *Org. Electron.* 82, 105701. <https://doi.org/10.1016/j.orgel.2020.105701>.
- Chang, L., Sheng, M., Duan, L., Uddin, A., 2021. Ternary organic solar cells based on non-fullerene acceptors: A review. *Org. Electron.* 90, 106063. <https://doi.org/10.1016/j.orgel.2021.106063>.
- Chen, Y., Wan, X., Long, G., 2013. High performance photovoltaic applications using solution-processed small molecules. *Acc. Chem. Res.* 46 (11), 2645–2655. <https://doi.org/10.1021/ar400088c>.
- Collins, S.D., Ran, N.A., Heiber, M.C., Nguyen, T.-Q., 2017. Small is powerful: recent progress in solution-processed small molecule solar cells. *Adv. Energy Mater.* 7, 1602242. <https://doi.org/10.1002/aenm.201602242>.
- Doumon, N.Y., Houard, F.V., Dong, J., Yao, H., Portale, G., Hou, J., Koster, L.J.A., 2019. Energy level modulation of ITIC derivatives: Effects on the photodegradation of conventional and inverted organic solar cells. *Org. Electron.* 69, 255–262. <https://doi.org/10.1016/j.orgel.2019.03.037>.
- Duan, T., Gao, J., Xu, T., Kan, Z., Chen, W., Singh, R., Kini, G.P., Zhong, C., Yu, D., Xiao, Z., Xiao, Z., Lu, S., 2020. Simple organic donors based on halogenated oligothiophenes for all small molecule solar cells with efficiency over 11%. *J. Mater. Chem. A* 8 (12), 5843–5847. <https://doi.org/10.1039/D0TA00159G>.
- Farahat, M.E., Tsao, C.-S., Huang, Y.-C., Chang, S.H., Budiawan, W., Wu, C.-G., Chu, C.-W., 2016. Toward environmentally compatible molecular solar cells processed from halogen-free solvents. *J. Mater. Chem. A* 4 (19), 7341–7351. <https://doi.org/10.1039/C6TA01368F>.
- Feng, H., Qiu, N., Wang, X., Wang, Y., Kan, B., Wan, X., Zhang, M., Xia, A., Li, C., Liu, F., Zhang, H., Chen, Y., 2017. An A-D-A type small-molecule electron acceptor with end-extended conjugation for high performance organic solar cells. *Chem. Mater.* 29 (18), 7908–7917. <https://doi.org/10.1021/acs.chemmater.7b02811>.
- Fitzner, R., Mena-Osteritz, E., Mishra, A., Schulz, G., Reinold, E., Weil, M., Körner, C., Ziehke, H., Elschner, C., Leo, K., Riede, M., Pfeiffer, M., Uhrich, C., Bäuerle, P., 2012. Correlation of π -conjugated oligomer structure with film morphology and organic solar cell performance. *J. Am. Chem. Soc.* 134 (27), 11064–11067. <https://doi.org/10.1021/ja302320c>.
- Ge, J., Hong, L., Song, W., Xie, L., Zhang, J., Chen, Z., Yu, K., Peng, R., Zhang, X., Ge, Z., 2021. Solvent annealing enables 15.39% efficiency all-small-molecule solar cells through improved molecule interconnection and reduced non-radiative loss. *Adv. Energy Mater.* 11 (22), 2100800. <https://doi.org/10.1002/aenm.v11.2210.1002/aenm.202100800>.
- Gu, X., Zhou, Y., Gu, K., Kurosawa, T., Guo, Y., Li, Y., Lin, H., Schroeder, B.C., Yan, H., Molina-Lopez, F., Tassone, C.J., Wang, C., Mannsfeld, S.C.B., Yan, H.-e., Zhao, D., Toney, M.F., Bao, Z., 2017. Roll-to-roll printed large-area all-polymer solar cells with 5% efficiency based on a low crystallinity conjugated polymer blend. *Adv. Energy Mater.* 7 (14), 1602742. <https://doi.org/10.1002/aenm.v7.1410.1002/aenm.201602742>.
- Guijarro, F.G., Caballero, R., de la Cruz, P., Singhal, R., Langa, F., Sharma, G.D., 2020. Ternary all-small-molecule solar cells with two small-molecule donors and Y6 nonfullerene acceptor with a power Conversion efficiency over above 14% processed from a nonhalogenated solvent. *Sol. RRL* 4 (11), 2000460. <https://doi.org/10.1002/solr.v4.1110.1002/solr.202000460>.
- Hau, S.K., Yip, H.-L., Baek, N.S., Zou, J., O'Malley, K., Jen, A.-K.-Y., 2008. Air-stable inverted flexible polymer solar cells using zinc oxide nanoparticles as an electron selective layer. *Appl. Phys. Lett.* 92, 253301. <https://doi.org/10.1063/1.2945281>.
- Heo, Y.-J., Jung, Y.-S., Hwang, K., Kim, J.-E., Yeo, J.-S., Lee, S., Jeon, Y.-J., Lee, D., Kim, D.-Y., 2017. Small molecule organic photovoltaic modules fabricated via halogen-free solvent system with roll-to-roll compatible scalable printing method. *ACS Appl. Mater. Interfaces* 9 (45), 39519–39525. <https://doi.org/10.1021/acsami.7b12420>.
- Huang, Y.-C., Chia, H.-C., Chuang, C.-M., Tsao, C.-S., Chen, C.-Y., Su, W.-F., 2013. Facile hot solvent vapor annealing for high performance polymer solar cell using spray process. *Sol. Energy Mater. Sol. Cells* 114, 24–30. <https://doi.org/10.1016/j.solmat.2013.02.022>.
- Huang, Y.-C., Tsao, C.-S., Huang, T.-Y., Cha, H.-C., Patra, D., Su, C.-J., Jeng, U.-S., Ho, K.-C., Wei, K.-H., Chu, C.-W., 2015. Quantitative characterization and mechanism of formation of multilength-scale bulk heterojunction structures in highly efficient solution-processed small-molecule organic solar cells. *J. Phys. Chem. C* 119 (29), 16507–16517. <https://doi.org/10.1021/acs.jpcc.5b05239>.
- Huang, Y.-C., Cha, H.-C., Chen, C.-Y., Tsao, C.-S., 2016. Morphological control and performance improvement of organic photovoltaic layer of roll-to-roll coated polymer solar cells. *Sol. Energy Mater. Sol. Cells* 150, 10–18. <https://doi.org/10.1016/j.solmat.2016.01.042>.

- Jiang, M., Bai, H., Zhi, H., Yan, L., Woo, H.Y., Tong, L., Wang, J., Zhang, F., An, Q., 2021. Rational compatibility in a ternary matrix enables all-small-molecule organic solar cells with over 16% efficiency. *Energy Environ. Sci.* 14 (7), 3945–3953. <https://doi.org/10.1039/D1EE00496D>.
- Kan, B., Li, M., Zhang, Q., Liu, F., Wan, X., Wang, Y., Ni, W., Long, G., Yang, X., Feng, H., Zuo, Y.I., Zhang, M., Huang, F., Cao, Y., Russell, T.P., Chen, Y., 2015. A series of simple oligomer-like small molecules based on oligothiophenes for solution-processed solar cells with high efficiency. *J. Am. Chem. Soc.* 137 (11), 3886–3893. <https://doi.org/10.1021/jacs.5b00305>.
- Krebs, F.C., Gevorgyan, S.A., Alstrup, J., 2009. A roll-to-roll process to flexible polymer solar cells: model studies, manufacture and operational stability studies. *J. Mater. Chem.* 19, 5442–5451. <https://doi.org/10.1039/B823001C>.
- Kyaw, A.K.K., Wang, D.H., Luo, C., Cao, Y., Nguyen, T.-Q., Bazan, G.C., Heeger, A.J., 2014. Effects of solvent additives on morphology, charge generation, transport, and recombination in solution-processed small-molecule solar cells. *Adv. Energy Mater.* 4, 1301469. <https://doi.org/10.1002/aenm.201301469>.
- Lechène, B.P., Cowell, M., Pierre, A., Evans, J.W., Wright, P.K., Arias, A.C., 2016. Organic solar cells and fully printed super-capacitors optimized for indoor light energy harvesting. *Nano Energy* 26, 631–640. <https://doi.org/10.1016/j.nanoen.2016.06.017>.
- Lee, S., Jeong, D., Kim, C., Lee, C., Kang, H., Woo, H.Y., Kim, B.J., 2020. Eco-friendly polymer solar cells: advances in green-solvent processing and material design. *ACS Nano* 14 (11), 14493–14527. <https://doi.org/10.1021/acsnano.0c07488>.
- Lee, C.J., Jradi, F.M., Mitchell, V.D., White, J., McNeill, C.R., Subbiah, J., Marder, S., Jones, D.J., 2020. A structural study of p-type A-D-A oligothiophenes: effects of regioregular alkyl sidechains on annealing processes and photovoltaic performances. *J. Mater. Chem. C* 8 (2), 567–580. <https://doi.org/10.1039/C9TC05280A>.
- Lee, H.K.H., Wu, J., Barbé, J., Jain, S.M., Wood, S., Speller, E.M., Li, Z., Castro, F.A., Durrant, J.R., Tsoi, W.C., 2018. Organic photovoltaic cells – promising indoor light harvesters for self-sustainable electronics. *J. Mater. Chem. A* 6, 5618–5626. <https://doi.org/10.1039/C7TA10875C>.
- Li, Q., Wang, L.-M., Liu, S., Guo, L., Dong, S., Ma, G., Cao, Z., Zhan, X., Gu, X., Zhu, T., Cai, Y.-P., Huang, F., 2020. Vertical composition distribution and crystallinity regulations enable high-performance polymer solar cells with >17% efficiency. *ACS Energy Lett.* 5, 3637–3646. <https://doi.org/10.1021/acsenerylett.0c01927>.
- Liao, H.-C., Tsao, C.-S., Huang, Y.-C., Jao, M.-H., Tien, K.-Y., Chuang, C.-M., Chen, C.-Y., Su, C.-J., Jeng, U.-S., Chen, Y.-F., Su, W.-F., 2014. Insights into solvent vapor annealing on the performance of bulk heterojunction solar cells by a quantitative nanomorphology study. *RSC Adv.* 4, 6246–6253. <https://doi.org/10.1039/C3RA45619F>.
- Lin, Y., Dam, H.F., Andersen, T.R., Bundgaard, E., Fu, W., Chen, H., Krebs, F.C., Zhan, X., 2013. Ambient roll-to-roll fabrication of flexible solar cells based on small molecules. *J. Mater. Chem. C* 1, 8007–8010. <https://doi.org/10.1039/C3TC31708K>.
- Lin, Y., Magomedov, A., Firdaus, Y., Kaltsas, D., El-Labban, A., Faber, H., Naphade, D.R., Yengel, E., Zheng, X., Yarali, E., Chaturvedi, N., Loganathan, K., Gkeka, D., AlShammari, S.H., Bakr, O.M., Laqual, V., Tsetsris, L., Getautis, V., Anthopoulos, T. D., 2018. Organic solar cells using a high ionization energy self-assembled monolayer as hole extraction interlayer. *ChemSusChem*, 10.1002/cssc.202100707.
- Liu, Q., Jiang, Y., Jin, K.e., Qin, J., Xu, J., Li, W., Xiong, J.i., Liu, J., Xiao, Z., Sun, K., Yang, S., Zhang, X., Ding, L., 2020. 18% efficiency organic solar cells. *Sci. Bull.* 65 (4), 272–275. <https://doi.org/10.1016/j.scib.2020.01.001>.
- Liu, C.-M., Su, M.-S., Jiang, J.-M., Su, Y.-W., Su, C.-J., Chen, C.-Y., Tsao, C.-S., Wei, K.-H., 2013. Distribution of crystalline polymer and fullerene clusters in both horizontal and vertical directions of high-efficiency bulk heterojunction solar cells. *ACS Appl. Mater. Interfaces* 5 (12), 5413–5422. <https://doi.org/10.1021/am4011995>.
- Löhner, F.C., Senfter, C., Schaffer, C.J., Schlöpf, J., González, D.M., Zhang, P., Roth, S.V., Müller-Buschbaum, P., 2020. Light-induced and oxygen-mediated degradation processes in photoactive layers based on PTB7-Th. *Adv. Photonics Res.* 1, 2000047. <https://doi.org/10.1002/adpr.202000047>.
- Love, J.A., Proctor, C.M., Liu, J., Takacs, C.J., Sharenko, A., van der Poll, T.S., Heeger, A. J., Bazan, G.C., Nguyen, T.-Q., 2013. Film morphology of high efficiency solution-processed small-molecule solar cells. *Adv. Funct. Mater.* 23 (40), 5019–5026. <https://doi.org/10.1002/adfm.v23.4010.1002/adfm.201300099>.
- Ma, R., Liu, T., Luo, Z., Gao, K.e., Chen, K., Zhang, G., Gao, W., Xiao, Y., Lau, T.-K., Fan, Q., Chen, Y., Ma, L.-K., Sun, H., Cai, G., Yang, T., Lu, X., Wang, E., Yang, C., Jen, A.-Y., Yan, H.e., 2020. Adding a third component with reduced miscibility and higher LUMO level enables efficient ternary organic solar cells. *ACS Energy Lett.* 5 (8), 2711–2720. <https://doi.org/10.1021/acsenerylett.0c0136410.1021/acsenerylett.0c01364.s001>.
- Mateker, William R., Heumueller, Thomas, Cheacharoen, Rongrong, Sachs-Quintana, I. T., Warman, Julien, Liu, Xiaofeng, Bazan, Guillermo C., Beaujuge, Pierre M., McGehee, Michael D., 2015. Molecular packing and arrangement govern the photo-oxidative stability of organic photovoltaic materials. *Chem. Mater.* 27(18), 6345–6353. <https://doi.org/10.1021/acs.chemmater.5b02341>.
- Min, J., Jiao, X., Sgobba, V., Kan, B., Heumueller, T., Rechberger, S., Speicker, E., Guldi, D.M., Wan, X., Chen, Y., Ade, H., Brabec, C.J., 2016. High efficiency and stability small molecule solar cells developed by bulk microstructure fine-tuning. *Nano Energy* 28, 241–249. <https://doi.org/10.1016/j.nanoen.2016.08.047>.
- Min, J., Jiao, X., Ata, I., Osvet, A., Ameri, T., Bäuerle, P., Ade, H., Brabec, C.J., 2016. Time-dependent morphology evolution of solution-processed small molecule solar cells during solvent vapor annealing. *Adv. Energy Mater.* 6, 1502579. <https://doi.org/10.1002/aenm.201502579>.
- Min, J., Güldal, N.S., Guo, J., Fang, C., Jiao, X., Hu, H., Heumueller, T., Ade, H., Brabec, C. J., 2017. Gaining further insight into the effects of thermal annealing and solvent vapor annealing on time morphological development and degradation in small molecule solar cells. *J. Mater. Chem. A* 5 (34), 18101–18110. <https://doi.org/10.1039/C7TA04769J>.
- Min, J., Luponosov, Y.N., Cui, C., Kan, B., Chen, H., Wan, X., Chen, Y., Ponomarenko, S. A., Li, Y., Brabec, C.J., 2017. Evaluation of electron donor materials for solution-processed organic solar cells via a novel figure of merit. *Adv. Energy Mater.* 7 (18), 1700465. <https://doi.org/10.1002/aenm.201700465>.
- Miranda, B.H.S., Correia, L. de Q., Soares, G.A., Martins, J.L., Lopes, P.L., Vilela, M.L., Rodrigues, J.F., Cunha, T.G., Vilaça, R. de Q., Castro-Hermosa, S., Wouk, L., Bagnis, D., 2021. Efficient fully roll-to-roll coated encapsulated organic solar module for indoor applications. *Solar Energy* 220, 343–353. <https://doi.org/10.1016/j.solener.2021.03.025>.
- Pan, M.-A., Lau, T.-K., Tang, Y., Wu, Y.-C., Liu, T., Li, K., Chen, M.-C., Lu, X., Ma, W., Zhan, C., 2019. 16.7%-efficiency ternary blended organic photovoltaic cells with PCBM as the acceptor additive to increase the open-circuit voltage and phase purity. *J. Mater. Chem. A* 7 (36), 20713–20722. <https://doi.org/10.1039/C9TA06929A>.
- Park, S.Y., Li, Y., Kim, J., Lee, T.H., Walker, B., Woo, H.Y., Kim, J.Y., 2018. Alkoxybenzothiadiazole-based fullerene and nonfullerene polymer solar cells with high shunt resistance for indoor photovoltaic applications. *ACS Appl. Mater. Interfaces* 10, 3885–3894. <https://doi.org/10.1063/1.4913589>.
- Perthue, A., Dominguez, I.F., Verstappen, P., Maes, W., Dautel, O.J., Wantz, G., Rivaton, A., 2018. An efficient and simple tool for assessing singlet oxygen involvement in the photo-oxidation of conjugated materials. *Sol. Energy Mater. Sol. Cells* 176, 336–339. <https://doi.org/10.1016/j.solmat.2017.10.019>.
- Proctor, C.M., Nguyen, T.-Q., 2015. Effect of leakage current and shunt resistance on the light intensity dependence of organic solar cells. *Appl. Phys. Lett.* 106, 083301.
- Qin, J., An, C., Zhang, J., Ma, K., Yang, Y., Zhang, T., Li, S., Xian, K., Cui, Y., Tang, Y., Ma, W., Yao, H., Zhang, S., Xu, B., He, C., Hou, J., 2020. 15.3% efficiency all-small-molecule organic solar cells enabled by symmetric phenyl substitution. *Sci. China Mater.* 63, 1142–1150. <https://doi.org/10.1007/s40843-020-1269-9>.
- Ramírez-Como, M., Sacramento, A., Sánchez, J.G., Estrada, M., Pallarés, J., Balderrama, V.S., Marsal, L.F., 2021. Small molecule organic solar cells toward improved stability and performance for indoor light harvesting application. *Sol. Energy Mater. Sol. Cells* 230, 111265. <https://doi.org/10.1016/j.solmat.2021.111265>.
- Søndergaard, R., Hösel, M., Angmo, D., Larsen-Olsen, T.T., Krebs, F.C., 2012. Roll-to-roll fabrication of polymer solar cells. *Mater. Today* 15 (1–2), 36–49. [https://doi.org/10.1016/S1369-7021\(12\)70019-6](https://doi.org/10.1016/S1369-7021(12)70019-6).
- Song, J., Ye, L., Li, C., Xu, J., Chandrabose, S., Weng, K., Cai, Y., Xie, Y., O'Reilly, P., Chen, K., Zhou, J., Zhou, Y.i., Hodgkiss, J.M., Liu, F., Sun, Y., 2020. An optimized fibril network morphology enables high-efficiency and ambient-stable polymer solar cells. *Adv. Sci.* 7 (18), 2001986. <https://doi.org/10.1002/advs.v7.1810.1002/advs.202001986>.
- Steim, R., Ameri, T., Schilinsky, P., Waldauf, C., Dennler, G., Scharber, M., Brabec, C.J., 2011. Organic photovoltaics for low light applications. *Sol. Energy Mater. Sol. Cells* 95, 3256–3261. <https://doi.org/10.1016/j.solmat.2011.07.011>.
- Wang, H., Xie, C., Zhang, W., Cai, S., Yang, Z., Gui, Y., 2007. Comparison of dye degradation efficiency using ZnO powders with various size scales. *J. Hazard. Mater.* 141 (3), 645–652. <https://doi.org/10.1016/j.jhazmat.2006.07.021>.
- Wessendorf, C.D., Schulz, G.L., Mishra, A., Kar, P., Ata, I., Weidelener, M., Urdampilleta, M., Hanisch, J., Mena-Osteritz, E., Lindén, M., Ahlswede, E., Bäuerle, P., 2014. Ahlswede and Peter Bäuerle, Efficiency improvement of solution-processed thienopyrrole-based A-D-A oligothiophene bulk-heterojunction solar cells by solvent vapor annealing. *Adv. Energy Mater.* 4 (14), 1400266. <https://doi.org/10.1002/aenm.201400266>.
- Xiao, L., Yan, C., Li, Z., Zhong, W., Tan, W., Liu, Y., Liu, F., Peng, X., Min, Y., 2021. Morphology evolution induced by sequential annealing enabling enhanced efficiency in all-small molecule solar cells. *ACS Appl. Energy Mater.* 4 (4), 4234–4241. <https://doi.org/10.1021/acsaem.1c0061710.1021/acsaem.1c00617.s001>.
- Yi, X., Ho, C.H.Y., Gautam, B., Lei, L., Chowdhury, A.H., Bahram, B., Qiao, Q., So, F., 2020. Effects of polymer crystallinity on non-fullerene acceptor based organic solar cell photostability. *J. Mater. Chem. C* 8, 16092–16099. <https://doi.org/10.1039/D0TC03969A>.
- Yin, H., Chen, S., Cheung, S.H., Li, H.W., Xie, Y., Tsang, S.W., Zhu, X., So, S.K.G., 2018. Porphyrin-based thick-film bulk-heterojunction solar cells for indoor light harvesting. *J. Mater. Chem. C* 6, 9111–9118. <https://doi.org/10.1039/C8TC02838A>.
- Yuan, J., Zhang, Y., Zhou, L., Zhang, G., Yip, H.-L., Lau, T.-K., Lu, X., Zhu, C., Peng, H., Johnson, P.A., Leclerc, M., Cao, Y., Ulanski, J., Li, Y., Zou, Y., 2019. Single-junction organic solar cell with over 15% efficiency using fused-ring acceptor with electron-deficient core. *Joule* 3 (4), 1140–1151. <https://doi.org/10.1016/j.joule.2019.01.004>.
- Yue, Q., Wu, H., Zhou, Z., Zhang, M., Liu, F., Zhu, X., 2019. 13.7% Efficiency Small-molecule solar cells enabled by a combination of material and morphology optimization. *Adv. Mater.* 31, 1904283. <https://doi.org/10.1002/adma.201904283>.
- Zhang, Y., Cho, Y., Lee, J., Oh, J., Kang, S.-H., Lee, S.M., Lee, B., Zhong, L., Huang, B., Lee, S., Lee, J.-W., Kim, B.J., Li, Y., Yang, C., 2020. Volatilizable and cost-effective quinone-based solid additives for improving photovoltaic performance and morphological stability in non-fullerene polymer solar cells. *J. Mater. Chem. A* 8 (26), 13049–13058. <https://doi.org/10.1039/D0TA04941G>.
- Zhang, L., Colella, N.S., Chermiawski, B.P., Mannsfeld, S.C.B., Briseno, A.L., 2014. Oligothiophene semiconductors: synthesis, characterization, and applications for organic devices. *ACS Appl. Mater. Interfaces* 6 (8), 5327–5343. <https://doi.org/10.1021/am406046h>.
- Zhang, C., Luo, Q., Wu, H., Li, H., Lai, J., Ji, G., Yan, L., Wang, X., Zhang, D., Lin, J., Chen, L., Yang, J., Ma, C., 2017. Roll-to-roll micro-gravure printed large-area zinc

oxide thin film as the electron transport layer for solution-processed polymer solar cells. *Org. Electron.* 45, 190–197. <https://doi.org/10.1016/j.orgel.2017.03.015>.